Axion optical induction of antiferromagnetic order

Jian-Xiang Qiu,[1] Christian Tzschaschel,[1] Junyeong Ahn,[2] Anyuan Gao,[1] Houchen Li,[1] Xin-Yue Zhang,[3] Barun Ghosh,[4] Chaowei Hu,[5] Yu-Xuan Wang,[3] Yu-Fei Liu,[1,2] Damien Bérubé,[1] Thao Dinh,[2,1] Zhenhao Gong,[6] Shang-Wei Lien,[7] Sheng-Chin Ho,[1] Bahadur Singh,[4] Kenji Watanabe,[8] Takashi Taniguchi,[9] David C. Bell,[10,11] Hai-Zhou Lu,[6] Arun Bansil,[4] Hsin Lin,[12] Tay-Rong Chang,[7] Brian B. Zhou,[3] Qiong Ma,[3] Ashvin Vishwanath,[2] Ni Ni*,[5] and Su-Yang Xu*[1]

[1] *Department of Chemistry and Chemical Biology, Harvard University, Massachusetts 02138, USA*

[2] *Department of Physics, Harvard University, Cambridge, MA 02138, USA*

[3] *Department of Physics, Boston College, Chestnut Hill, MA, USA*

[4] *Department of Physics, Northeastern University, Boston, MA 02115, USA*

[5] *Department of Physics and Astronomy and California NanoSystems Institute, University of California, Los Angeles, Los Angeles, CA 90095, USA.*

[6] *Shenzhen Institute for Quantum Science and Engineering and Department of Physics, Southern University of Science and Technology (SUSTech), Shenzhen 518055, China*

[7] *Department of Physics, National Cheng Kung University, Tainan 701, Taiwan*

[8] *Research Center for Functional Materials, National Institute for Materials Science, 1-1 Namiki, Tsukuba 305-0044, Japan*

[9] *International Center for Materials Nanoarchitectonics, National Institute for Materials Science, 1-1 Namiki, Tsukuba 305-0044, Japan*

[10] *Harvard John A. Paulson School of Engineering and Applied Sciences, Harvard University, Cambridge, Massachusetts 02138, USA*

[11] *Center for Nanoscale Systems, Harvard University,Cambridge, Massachusetts 02138, USA*

[12] *Institute of Physics, Academia Sinica, Taipei 11529, Taiwan*

(Dated: March 28, 2023)

* Corresponding authors (emails): suyangxu@fas.harvard.edu and nini@physics.ucla.edu

Using circularly-polarized light to control quantum matter is a highly intriguing topic in physics, chemistry and biology. Previous studies have demonstrated helicity-dependent optical control of spatial chirality and magnetization M. The former is central for asymmetric synthesis in chemistry and homochirality in bio-molecules, while the latter is of great interest for ferromagnetic spintronics. In this paper, we report the surprising observation of helicity-dependent optical control of fully-compensated antiferromagnetic (AFM) order in 2D even-layered $MnBi_2Te_4$, a topological Axion insulator with neither chirality nor M. We further demonstrate helicity-dependent optical creation of AFM domain walls by double induction beams and the direct reversal of AFM domains by ultrafast pulses. The control and reversal of AFM domains and domain walls by light helicity have never been achieved in any fully-compensated AFM. To understand this optical control, we study a novel type of circular dichroism (CD) proportional to the AFM order, which only appears in reflection but is absent in transmission. We show that the optical control and CD both arise from the optical Axion electrodynamics, which can be visualized as a Berry curvature real space dipole. Our Axion induction provides the possibility to optically control a family of $\mathcal{PT}$-symmetric AFMs such as Cr_2O_3, even-layered CrI_3 and possibly novel states in cuprates. In $MnBi_2Te_4$, this further opens the door for optical writing of dissipationless circuit formed by topological edge states.

Main

There is tremendous interest in finding innovative ways to control and manipulate complex quantum materials [1]. Antiferromagnets (AFMs) have zero net M, so AFM domains are immune to perturbing magnetic field. This leads to the prospect of robust magnetic storage [2, 3]. However, this robustness also means that manipulating fully-compensated AFM order is extremely difficult [3–6] (discussion in SI.V.2). As such, controlling AFM order has been recognized a key challenge toward the AFM spintronics [2, 3]. One known approach is to use the parallel E and B fields [7–9]. Compared to such electrical approach, optical control is non-contact, flexible, has good spatial resolution and further allows for ultrafast manipulation. It also enables fundamental understanding of the interaction of photons with charges, spins, lattice, and quantum geometry.

In this paper, we explore the novel possibility of controlling fully-compensated AFM order by circularly-polarized light, which has never been achieved. We got inspirations from (1) discoveries of helicity-dependent optical control of chiral materials and magnetization M [4, 10, 11] and (2) previous experiments reporting novel circular dichroism (CD) proportional to the AFM order in Cr_2O_3 [12, 13] and the pseudo-gap state of cuprates [14]. We report helicity-dependent optical control of fully-compensated AFM order induced by the optical Axion electrodynamics in even-layered $MnBi_2Te_4$.

$MnBi_2Te_4$, the first intrinsic magnetic topological insulator recently synthesized in 2019, has attracted great interest as it bridges three primary fields in quantum condensed matter: topology, magnetism and 2D van der Waals (vdW) materials [9, 15–28]. $MnBi_2Te_4$'s lattice consists of septuple layers (SL) separated by vdW gaps. Its magnetic ground state is layered AFM, which can be further tuned into a ferromagnetic state by a large B field (Fig. 1**e**). Previous theoretical works have comprehensively studied the electronic, magnetic and topological properties of $MnBi_2Te_4$ bulk and thin films (SI.V.3) [15–20]. The 2D magnetic and topological ground states can be classified into two kinds. The first kind has an obvious, nonzero static M hosting the Chern insulator state [9, 21–27]. It includes odd-layered $MnBi_2Te_4$ near $B = 0$ as well as odd-layered and even-layered $MnBi_2Te_4$ under large B fields. By contrast, the second, more special kind is the even-layered AFM $MnBi_2Te_4$, which will be our focus. It is expected to host fully-compensated AFM with an Axion insulator state [16, 17, 20–22] near $B = 0$.

Our magneto-optical setup (Fig. 1**f**) allows us to investigate the interaction between circularly-polarized light and quantum materials by probing CD, the difference between σ^+ and σ^- light. Importantly, our setup can measure CD both in the reflection and transmission channels and has a supercontinuum light source with tunable wavelength (500 nm to 1000 nm). These capabilities are crucial for our findings, including unique helicity-dependence, wavelength-dependence, and reflection and transmission properties. The measurement temperature is 2 K unless noted otherwise.

Optical induction in a 2D topological antiferromagnet

In this section, we show the observation of optical induction at specific wavelengths. Systematic wavelength dependences will be presented later. As shown in Fig. 2**a**, starting from $T = 30$ K, we shine σ^+ circularly-polarized light ($\lambda_{\text{induction}} = 840$ nm, $P_{\text{induction}} \simeq 1$ mW) onto a spot on a 8SL $MnBi_2Te_4$ flake (sample-S1, see Fig. 2**e**) while lowering its temperature. Upon reaching 2 K, we turn off the induction light and measure the reflection CD (RCD) with the detection light ($\lambda_{\text{detection}} = 946$ nm and $P_{\text{detection}} \simeq 30$ μW). We observe significant anomalous RCD at $B = 0$ (Fig. 2**c**). We then measure the anomalous RCD while warming up. The RCD vanishes above T_{N}. From $T = 30$ K, we repeat the same induction process (Fig. 2**b**) only changing the induction helicity to σ^-. We turn off the induction light at 2 K and repeat the measurements. Remarkably, the global sign of RCD data is reversed (Fig. 2**d**). We repeated the induction nine consecutive times (Figs. 2**e-g** and Extended Data Fig. 4). We find that the RCD at 2 K is consistently controlled by the induction light helicity. On the other hand, when cooling down without induction light, we still observe the anomalous RCD. Only the sign is random (SI.Fig. S17).

Understanding the optical induction by investigating the anomalous CD

Because the anomalous RCD correlates with the AFM order, the data above hint an exciting possibility that induction helicity can control the AFM order in 8SL $MnBi_2Te_4$. To understand this optical induction, we first investigate the anomalous CD, because it serves as the experimental indicator of the AFM order. Here, we focus on sample-S2 on a diamond substrate, which consists of four connected flakes of $5-8$ SLs (Extended Data Fig. 5**a**). We performed systematic RCD measurements (Extended Data Figs. 5**c-p**). In 5SL and 7SL, we observed the conventional magnetic CD proportional to M. In 6SL and 8SL, we observed the anomalous RCD. We have further confirmed the reproducibility of the anomalous CD in more than 10 samples.

There are two possibilities for the anomalous RCD. (1) It can be the magnetic CD proportional to M (we will explain the origin of M below); (2) Actually, in the absence of any M, there can be an AFM CD unrelated to M but proportional to the AFM order L in $\mathcal{PT}$ symmetric AFMs as reported in Cr_2O_3 [12, 13] (this is symmetry allowed see SI.III), which is also likely the origin of the CD observed in the pseudogap of cuprates [14, 29, 30]. One may think that (1) and (2) can be easily discerned because they are proportional to different order parameters. But in reality this is often not feasible, because the M in an AFM is typically coupled with the AFM order L. For example, suppose our sample is subject to a fixed vertical, static electric field E_z due to substrate, which in turn generates an M due to the static ME coupling α, i.e., $M = \alpha E_z$. Because the two AFM states have opposite α, if one flips the AFM order L, M will also flip. In fact, the induced M turned out to be the dominant mechanism for RCD in even-layered CrI_3 [8, 31]. Therefore, new measurements beyond the RCD are crucial to distinguish the above two possibilities.

We now proceed to show that CD in transmission, i.e., TCD, provides the decisive new measurement, as proposed in Ref. [32, 33]. Magnetic CD is known to also occur in transmission channel (just like the Faraday effect). By contrast, the AFM CD has TCD = 0 because of $\mathcal{PT}$ symmetry. Extended Data Fig. 6**a** describes a conceptual experiment with σ^- light transmitting through sample. Upon $\mathcal{PT}$ inversion, the even-layered $MnBi_2Te_4$ remains invariant and light path also stays the same, but light helicity is reversed. As such, $\mathcal{PT}$ enforces the transmission coefficients for $\sigma^\pm$ light to be identical, which means TCD = 0 (similar analysis can show that RCD is allowed, Extended Data Fig. 6**b**). Therefore, what truly distinguishes the AFM CD from the magnetic CD is TCD = 0.

As such, we study TCD and RCD simultaneously in sample-S3, which consists of 5SL and 6SL on diamond (Fig. 3). In 5SL, the magnetic CD indeed shows up prominently in both reflection and transmission. We now turn to 6SL. At 946 nm where significant anomalous RCD was observed at $B = 0$ (Fig. 3**b**), the TCD, by contrast, is zero. Continuous wavelength dependence (Fig. 3**c**) shows that, strikingly, TCD is negligibly small over the entire spectrum. Also, we have repeated the RCD *vs*. TCD experiments in sample-S1 (Extended Data Fig. 7), on which the induction experiments were performed. In SI.II.1, we show additional data to further substantiate this. Therefore, we showed that the anomalous RCD in even-layered $MnBi_2Te_4$ only appears in reflection but is absent in transmission. Such unique reflection and transmission characters, although has been long proposed in theory [32], have never been observed before, allowing us to rule out the magnetic CD due to uncompensated M. As such, the anomalous RCD in even-layered $MnBi_2Te_4$ is the AFM CD. Below, we show that the AFM CD can be further categorized by the microscopic mechanisms and our results provide the first demonstration of the optical Axion mechanism.

CD arising from the optical Axion electrodynamics

The AFM CD arises from the diagonal optical ME coupling $\alpha(\omega)_{ii}$ [12, 32], but the optical ME coupling has different components corresponding to different microscopic mechanisms. Specifically, the traceless part of $\alpha(\omega)_{ii}$ is known as the gyrotropic birefringence (GB) [$\text{GB} = \frac{1}{3}(\alpha(\omega)_{xx} - \alpha(\omega)_{zz})$] [34, 35]; while the trace part is the Axion contribution $\theta(\omega) = \frac{1}{3}\sum_i \alpha(\omega)_{ii} = \frac{1}{3}[2\alpha(\omega)_{xx} + \alpha(\omega)_{zz}]$ (we have applied $\alpha(\omega)_{xx} = \alpha(\omega)_{yy}$ because of $MnBi_2Te_4$'s C_{3z} symmetry). However, for a long time, only the GB (traceless part) was theoretically derived [34]. Only very recently, the theory of Axion electrodynamics at optical frequencies was developed [33], which allows us to compute the Axion optical ME coupling in quasi-2D periodic systems (see Methods for expressions). In bulk $MnBi_2Te_4$, its AFM respects inversion symmetry, so the GB contribution is expected to vanish, allowing us to isolate the Axion contribution. Interestingly, even for few-layered $MnBi_2Te_4$ where both Axion and GB are allowed by symmetry, our DFT calculations show that Axion $\theta(\omega)$ strongly dominates (e.g. Fig. 3**f** for 6SL $MnBi_2Te_4$). Further theoretical studies are needed to understand why Axion dominates over GB in few-layered $MnBi_2Te_4$. As shown in Fig. 3**e**, the physics of Axion ME coupling can be visualized by a Berry curvature real space dipole (see derivation in the Methods): Because the top and bottom surfaces have opposite Berry curvature, by applying E field, they feature opposite Hall currents. In fact, if one considers the Hall currents on all four facets parallel to E field, one naturally obtains a circulating current, which leads to an M. This physical picture works for both static and optical Axion ME effects. We only need the following correspondence: the static $E \leftrightarrow$ optical E^{ω} and Berry curvature $\leftrightarrow$ inter-band Berry curvature. We note that, in contrast to the static limit, for our photon energy (500 − 1000 nm), the optical transition involves many bands, not just the topological surface states; and the contributions from the higher bands are more significant (SI.IV.2).

Using the calculated $\theta(\omega)$, we can theoretically compute the Axion CD (see expressions in SI.IV.1), and thus compare it with the experimental RCD data. As shown in Figs. 3**c,g**, we observe good agreement between experimental RCD data and calculated Axion CD in terms of the magnitude and the spectral shape. By contrast, the GB-induced CD is too small to account for the data. In SI.I.3, we provide further systematic studies to carefully address the light-attenuation-induced CD: In a layered AFM, every adjacent layer gives opposite magnetic CD. Therefore, as the light attenuates layer by layer, the absorption can lead to an uncompensated RCD signal [36]. We address this possibility by systematically analyzing the RCD amplitude and spectrum. Based on above data and calculations, we conclude that the optical Axion ME coupling is the most likely origin. In future, it would be of great interest to extend the study to terahertz, where we expect a finite Kerr rotation in fully-compensated even-layered $MnBi_2Te_4$ from which one can obtain the quantized Axion ME coupling [33]; meanwhile there is zero RCD due to no absorption and zero Faraday due to $\mathcal{PT}$ symmetry.

Optical induction arising from the optical Axion electrodynamics

Our simultaneous RCD and TCD measurements demonstrated that the M in even-layered $MnBi_2Te_4$ is negligibly small. Instead, circularly-polarized light with opposite helicity couples differently to the opposite AFM domains. To further confirm that this is also the origin of the optical induction, we now investigate its wavelength dependence. In particular, we notice that the RCD data has distinct spectral dependence (Fig. 3**c**): E.g. RCD at 840 nm and 540 nm have opposite signs. Therefore, if the induction has the same physical origin as the CD, i.e., the optical Axion electrodynamics, then the induction effects using $\lambda_{\text{induction}} = 840$ nm and $\lambda_{\text{induction}} = 540$ nm should be opposite. Specifically, with the same light helicity, the induction using $\lambda_{\text{induction}} = 840$ nm and $\lambda_{\text{induction}} = 540$ nm should lead to opposite AFM domains. As such, we carry out the induction with $\lambda_{\text{induction}} = 540$ nm and 840 nm (note that $\lambda_{\text{detection}}$ is fixed to achieve consistent comparison). By directly comparing Fig. 4**a,c** ($\lambda_{\text{induction}} = 540$ nm) and Fig. 4**b,d** ($\lambda_{\text{induction}} = 840$ nm), we indeed find that the results are entirely opposite (see free energy analysis in Fig. 4**f**). We further study the induction at other wavelengths. As shown in Fig. 4**e**, our data show that the effect of induction at 540 nm and 580 nm is opposite to that of 740 nm, 840 nm and 946 nm. These results are consistent with the sign of the RCD spectra for even-layered $MnBi_2Te_4$, which provide strong evidence that the induction and CD share the same physical origin, i.e., the optical Axion electrodynamics. Therefore, we conclude on the observation of the Axion induction, i.e., helicity-dependent control of fully-compensated AFM order based on the optical Axion electrodynamics.

Optical creation of AFM domain wall by double induction

The control of AFM order with light helicity makes it possible to spatially modulate the AFM domain structure. For instance, one can think of creating AFM domain wall using two close-by light beams of opposite helicity. Here, we demonstrate this possibility in a 8SL flake (sample-S5). As shown in Fig. 5**a**, the two light beams are spatially separated and their polarizations can be controlled separately. When both beams are σ^+ polarized (Fig. 5**c**), the double induction yields one AFM domain, similar to the single induction before. We then change the two beams to σ^+ and σ^- (Fig. 5**d**). Indeed, the double induction yields opposite AFM domains separated by a domain wall. If we further change the two beams to σ^- and σ^+, then both AFM domains are flipped and again an AFM domain wall is created. In SI.II.3, we show more systematic data. By double Axion induction, we achieve helicity-dependent optical creation of AFM domain wall for the first time.

Direct optical switching of AFM domain by ultrafast pulse

The optical induction requires warming up the entire sample and then cooling down across T_{N} with light. To achieve optical writing of complex AFM structures at will, direct optical switching would be highly desirable. We have achieved such direct optical switching of the AFM domain using ultrafast pulsed light with circular polarization. We start from the entire 8SL sample in a single AFM domain (Fig. 6), while the sample is kept at $T = 18$ K (below T_{N}). We shone ultrafast laser pulses with circular polarization, turned off the ultrafast laser, then checked the AFM order by RCD. As shown in Fig. 6, we indeed directly switch the AFM domain at the ultrafast laser spot with clear helicity dependence. In SI.II.4, we show more systematic data. Direct helicity-dependent optical switching of AFM has never been achieved before. This new result opens a pathway to photolithography for AFM structures.

Discussions

Our results have demonstrated a new type of helicity-dependent optical control (Extended Data Fig. 2): It has been previously known that the rotating electric field of circularly-polarized (CP) light serves as an effective $\mathbf{B}$ field [$(\mathbf{E}^* \times \mathbf{E})$ has the same symmetry as $\mathbf{B}$], while the rotating electric field multiplies the light propagation vector leads to an effective chiral force [$(\mathbf{E}^* \times \mathbf{E}) \cdot \hat{q}$ has the same symmetry as chirality]. Therefore, CP light can control magnetization M and chirality [4, 11]. In our work, we discovered that CP light can control the AFM order. Such new control can be visualized by the picture that CP light provides an effective Axion $\mathbf{E} \cdot \mathbf{B}$ field [$(\mathbf{E}^* \times \mathbf{E}) \cdot \hat{z}$ has the same symmetry as $\mathbf{E} \cdot \mathbf{B}$], where the rotating electric field of CP light serves as an effective B_z field and the sample surface normal as an effective E_z. Looking forward, we highlight the following future directions: First, our simultaneous RCD and TCD measurements realize a novel symmetry probe for both $\mathcal{T}$ and $\mathcal{PT}$, which is valuable to investigate novel $\mathcal{T}$-breaking phases in unconventional superconductors and charge orders. For instance, optical nonreciprocity (Kerr rotation) with nominally zero magnetization was also observed in unconventional superconductors such as UPt_3 [37–39]. A finite Kerr signal means $\mathcal{T}$-breaking. Whether this state preserves/breaks $\mathcal{PT}$ symmetry is unknown, which can be learnt by simultaneous transmission experiments. Interestingly, theory predicts exotic $\mathcal{PT}$-symmetric topological superconductivity [40]. Second, we note that the optical Axion $\theta(\omega)$ electrodynamics is quantum geometrical (i.e., it depends on the geometrical properties of Bloch wavefunction such as Berry curvature) but not topological. This is in contrast to the static θ [41, 42], which can lead to topological quantized effects with exciting experimental progress [22, 43–46]. This means that the optical $\theta(\omega)$ cannot be used to discern topology at photon energies larger than the band gap. On the flip side, it also makes this novel physics more widely applicable in other $\mathcal{PT}$-symmetric AFMs without mirror planes, including Cr_2O_3 and CrI_3 and even the pseudo-gap state of cuprates [14]. Third, the direct switching by ultrafast pulses (Fig. 6) is potentially on the ultrafast timescale. So future pump probe experiments to directly demonstrate ultrafast AFM reversal would be highly desirable. Finally, for $MnBi_2Te_4$, because the AFM order is directly coupled to the sign of static θ angle (a topological invariant) as well as the half-quantized surface Hall conductivity [16, 17, 20], our definitive, versatile optical control of AFM domains and domain walls also leads to an optical writing of ballistic circuits of topological chiral edge states.

---

[1] Basov, D., Averitt, R. & Hsieh, D. Towards properties on demand in quantum materials. *Nature Mater.* **16**, 1077–1088 (2017).

[2] Jungwirth, T., Marti, X., Wadley, P. & Wunderlich, J. Antiferromagnetic spintronics. *Nature Nanotech.* **11**, 231–241 (2016).

[3] Němec, P., Fiebig, M., Kampfrath, T. & Kimel, A. V. Antiferromagnetic opto-spintronics. *Nature Phys.* **14**, 229–241 (2018).

[4] Kirilyuk, A., Kimel, A. V. & Rasing, T. Ultrafast optical manipulation of magnetic order. *Rev. Mod. Phys.* **82**, 2731–2784 (2010).

[5] Manz, S. *et al.* Reversible optical switching of antiferromagnetism in $TbMnO_3$. *Nature Photon.* **10**, 653–656 (2016).

[6] Higuchi, T. & Kuwata-Gonokami, M. Control of antiferromagnetic domain distribution via polarization-dependent optical annealing. *Nature Commun.* **7**, 10720 (2016).

[7] Fiebig, M. Revival of the magnetoelectric effect. *Journal of Physics D: Applied Physics* **38**, R123–R152 (2005).

[8] Jiang, S., Shan, J. & Mak, K. F. Electric-field switching of two-dimensional van der Waals magnets. *Nature Mater.* **17**, 406–410 (2018).

[9] Gao, A. *et al.* Layer Hall effect in a 2D topological axion antiferromagnet. *Nature* **595**, 521–525 (2021).

[10] Huck, N. P., Jager, W. F., De Lange, B. & Feringa, B. L. Dynamic control and amplification of molecular chirality by circular polarized light. *Science* **273**, 1686–1688 (1996).

[11] Xu, S.-Y. *et al.* Spontaneous gyrotropic electronic order in a transition-metal dichalcogenide. *Nature* **578**, 545–549 (2020).

[12] Krichevtsov, B., Pavlov, V., Pisarev, R. & Gridnev, V. Spontaneous non-reciprocal reflection of light from antiferromagnetic Cr_2O_3. *J. Phys. Condens. Matter* **5**, 8233–8244 (1993).

[13] Krichevtsov, B., Pavlov, V., Pisarev, R. & Gridnev, V. Magnetoelectric spectroscopy of electronic transitions in antiferromagnetic Cr_2O_3. *Phys. Rev. Lett.* **76**, 4628–4631 (1996).

[14] Xia, J. *et al.* Polar Kerr-effect measurements of the high-temperature $YBa_2Cu_3O_{6+x}$ superconductor: evidence for broken symmetry near the pseudogap temperature. *Phys. Rev. Lett.* **100**, 127002 (2008).

[15] Otrokov, M. M. *et al.* Prediction and observation of an antiferromagnetic topological insulator. *Nature* **576**, 416–422 (2019).

[16] Otrokov, M. M. *et al.* Unique thickness-dependent properties of the van der waals interlayer antiferromagnet $MnBi_2Te_4$ films. *Phys. Rev. Lett.* **122**, 107202 (2019).

[17] Li, J. *et al.* Intrinsic magnetic topological insulators in van der Waals layered $MnBi_2Te_4$-family materials. *Science Advances* **5**, eaaw5685 (2019).

[18] Zhang, D. *et al.* Topological axion states in the magnetic insulator $MnBi_2Te_4$ with the quantized magnetoelectric effect. *Phys. Rev. Lett.* **122**, 206401 (2019).

[19] Zhang, R.-X., Wu, F. & Das Sarma, S. Möbius insulator and higher-order topology in $MnBi_{2n}Te_{3n+1}$. *Phys. Rev. Lett.* **124**, 136407 (2020).

[20] Liu, Z. & Wang, J. Anisotropic topological magnetoelectric effect in axion insulators. *Phys. Rev. B* **101**, 205130 (2020).

[21] Deng, Y. *et al.* Quantum anomalous Hall effect in intrinsic magnetic topological insulator $MnBi_2Te_4$. *Science* **367**, 895–900 (2020).

[22] Liu, C. *et al.* Robust axion insulator and Chern insulator phases in a two-dimensional antiferromagnetic topological insulator. *Nature Mater.* **19**, 522–527 (2020).

[23] Deng, H. *et al.* High-temperature quantum anomalous hall regime in a $MnBi_2Te_4/Bi_2Te_3$ superlattice. *Nature Phys.* **17**, 36–42 (2021).

[24] Yang, S. *et al.* Odd-even layer-number effect and layer-dependent magnetic phase diagrams in $MnBi_2Te_4$. *Phys. Rev. X* **11**, 011003 (2021).

[25] Ovchinnikov, D. *et al.* Intertwined topological and magnetic orders in atomically thin Chern insulator $MnBi_2Te_4$. *Nano Lett.* **21**, 2544–2550 (2021).

[26] Cai, J. *et al.* Electric control of a canted-antiferromagnetic Chern insulator. *Nature Commun.* **13**, 1668 (2022).

[27] Li, Y. *et al.* Nonlocal transport and one-dimensional conduction in the Axion insulator state of $MnBi_2Te_4$. Preprint at https://arxiv.org/abs/2105.10390 (2021).

[28] Tai, L. *et al.* Distinguishing two-component anomalous Hall effect from topological Hall effect in magnetic topological insulator $MnBi_2Te_4$. Preprint at https://arxiv.org/abs/2103.09878 (2021).

[29] Orenstein, J. Optical nonreciprocity in magnetic structures related to high-T_c superconductors. *Phys. Rev. Lett.* **107**, 067002 (2011).

[30] Varma, C. Gyrotropic birefringence in the underdoped cuprates. *Europhys. Lett.* **106**, 27001 (2014).

[31] Huang, B. *et al.* Electrical control of 2D magnetism in bilayer CrI_3. *Nature Nanotech.* **13**, 544–548 (2018).

[32] Canright, G. & Rojo, A. Ellipsometry and broken time-reversal symmetry in the high-temperature superconductors. *Phys. Rev. B* **46**, 14078 (1992).

[33] Ahn, J., Xu, S.-Y. & Vishwanath, A. Theory of optical axion electrodynamics and application to the kerr effect in topological antiferromagnets. *Nature Commun.* **13**, 7615 (2022).

[34] Malashevich, A. & Souza, I. Band theory of spatial dispersion in magnetoelectrics. *Phys. Rev. B* **82**, 245118 (2010).

[35] Graham, E. & Raab, R. Macroscopic theory of reflection from antiferromagnetic. *J. Phys.: Condens.*

Matter **9**, 1863–1869 (1997).

[36] Dzyaloshinskii, I. & Papamichail, E. Nonreciprocal optical rotation in antiferromagnets. *Phys. Rev. Lett.* **75**, 3004 (1995).

[37] Xia, J., Maeno, Y., Beyersdorf, P. T., Fejer, M. & Kapitulnik, A. High resolution polar Kerr effect measurements of Sr_2RuO_4: Evidence for broken time-reversal symmetry in the superconducting state. *Phys. Rev. Lett.* **97**, 167002 (2006).

[38] Schemm, E., Gannon, W., Wishne, C., Halperin, W. & Kapitulnik, A. Observation of broken time-reversal symmetry in the heavy-fermion superconductor UPt_3. *Science* **345**, 190–193 (2014).

[39] Hayes, I. *et al.* Multicomponent superconducting order parameter in UTe_2. *Science* **373**, 797–801 (2021).

[40] Kawabata, K., Ashida, Y., Katsura, H. & Ueda, M. Parity-time-symmetric topological superconductor. *Phys. Rev. B* **98**, 085116 (2018).

[41] Qi, X.-L., Hughes, T. L. & Zhang, S.-C. Topological field theory of time-reversal invariant insulators. *Phys. Rev. B* **78**, 195424 (2008).

[42] Essin, A. M., Moore, J. E. & Vanderbilt, D. Magnetoelectric polarizability and axion electrodynamics in crystalline insulators. *Phys. Rev. Lett.* **102**, 146805 (2009).

[43] Wu, L. *et al.* Quantized Faraday and Kerr rotation and axion electrodynamics of a 3D topological insulator. *Science* **354**, 1124–1127 (2016).

[44] Xiao, D. *et al.* Realization of the axion insulator state in quantum anomalous Hall sandwich heterostructures. *Phys. Rev. Lett.* **120**, 056801 (2018).

[45] Nenno, D. M., Garcia, C. A., Gooth, J., Felser, C. & Narang, P. Axion physics in condensed-matter systems. *Nature Rev. Phys.* **2**, 682–696 (2020).

[46] Mogi, M. *et al.* Experimental signature of the parity anomaly in a semi-magnetic topological insulator. *Nature Phys.* **18**, 390–394 (2022).

[47] Kimura, K., Katsuyoshi, T., Sawada, Y., Kimura, S. & Kimura, T. Imaging switchable magnetoelectric quadrupole domains via nonreciprocal linear dichroism. *Commun. Mater.* **1**, 39 ((2020)).

Methods

Crystal growth: Bulk crystals were grown by the flux method [48]. Elemental Mn, Bi and Te were mixed at a molar ratio of 15 : 170 : 270, and sealed in a quartz tube with argon environment. The ampule was first heated to 900°C for 5 hours. It was then moved to another furnace where it slowly cooled from 597°C to 587°C and stayed for one day at 587°C. Finally, $MnBi_2Te_4$ were obtained by centrifuging the ampule to separate the crystals from the Bi_2Te_3 flux.

Sample fabrication: To preserve the intrinsic properties of 2D $MnBi_2Te_4$ flakes, the entire device fabrication process was performed without exposure to air, chemicals, or heat in an Ar-filled glovebox with O_2 and water levels below 0.01 ppm. First, thin flakes were mechanically exfoliated on a 300-nm SiO_2/Si wafer. The number of layers was determined based on the optical contrast shown in Ref. [9]. Second, we picked up a desired $MnBi_2Te_4$ flake and transferred it onto a diamond, sapphire, or hBN substrate by the cryogenic pickup method developed in Ref. [49], where a thin piece of PDMS (polydimethylsiloxane) was cooled to $-110°$ by liquid nitrogen to achieve the pickup. Third, a $20-50$ nm hBN flake was transferred onto the $MnBi_2Te_4$ flake. A 200 nm layer of PMMA (poly(methyl methacrylate)) was spin-coated onto the sample to further protect it before transferring it from the glovebox to a cryostat.

Circular dichroism and optical induction: Optical CD measurements were performed in the closed-loop magneto-optical cryostat OptiCool by Quantum Design (base temperature ~ 2 K and B field ± 7 T) using a supercontinuum laser SuperK-EXR20 by NKT photonics (wavelength 500 nm to 2500 nm, pulse width ~ 12 ps at 1064 nm). We focused on $500-1000$ nm due to constraints of the photodetector, lens, objective and beam splitter. A spectrometer SpectraPro-300i by Acton Research was used to select the wavelength. The beam went through a photoelastic modulator (PEM200, Hinds instruments) operating at $\frac{\lambda}{4}$ retardation with a frequency of 50 kHz. After an optical chopper (1000 Hz) and a broadband plate beam-splitter (near normal, Thorlabs BSW26), the beam was focused onto the sample by a 50X Mitutoyo Plan Apochromat Objective (MY50X-825). The reflected beam went through the cryostat's top window, was collimated by the same objective, and was collected by a Si Avalanche Photodetector (APD410A, Thorlabs). The transmitted beam was collimated by a parabolic mirror (37-282 Edmund Optics) inside the cryostat and passed through a side window to reach the APD. The corresponding reflection and transmission APD signals were analyzed by two lock-in amplifiers at 50 kHz (the PEM frequency) and 1000 Hz (the chopper frequency), respectively. The RCD and TCD were the ratio of the 50 kHz and 1000 Hz signals. Spatial imaging were achieved using a galvo scanning mirror system. The background CD were obtained by performing the same measurement at a location immediately next to $MnBi_2Te_4$ flake (SI.II.1). In order to reduce the background CD, the beam splitter (BSW26, Thorlabs) was intentionally used at near normal incidence (Fig. 1**f**)

Induction experiments were performed using the same supercontinuum laser. The induction light shared the same beam path. When conducting induction experiments, the PEM was turned off. An achromatic $\frac{\lambda}{4}$ waveplate (AQWP10M-580, Thorlabs) was installed before the objective, which generates $\sigma^{\pm}$ polarization. After the induction was completed, the induction light was then turned off, and the $\lambda/4$ waveplate was removed from the beam path, allowing us to measure the CD using the PEM. In order to check if the phase of the signal was definitive and consistent, we deliberately turned off and on the PEM multiple times and took the identical measurements. Every time, the phase (sign) of the signal was consistent. We show the data and explain this based on the PEM instrumentation in SI.II.1.

The direct switching was achieved with the sample kept at $T = 18$ K (below $T_{\rm N} = 25$ K). The pulsed light was generated by an amplified Yb:KGW laser (Pharos, LightConversion) with pulse duration 168 fs, wavelength 1030 nm, repetition rate 100 kHz. The power applied on the sample was 0.04 mW (= 0.4 nJ per pulse). We shone the ultrafast light for 1min, turned it off, and then checked the AFM by RCD.

NV center magnetometry: NV center magnetic imaging was performed using a diamond sample containing a near-surface ensemble of NV centers. A green laser (515 nm, 100 μW power, beam spot FWHM 400 nm) was used to probe the optically-detected magnetic resonance across the NV ensemble [50]. A pulsed electron spin resonance measurement (500 ns pulse length) was performed on the $|0\rangle$ to $|1\rangle$ NV ground-state transition at a background field of 141 mT along the NV axis ($\sim$ 1.08 GHz). To determine the stray field dB due to the flake, a linear plane-fit background is subtracted from the raw field image. The NV detection limit was about $2\mu_{\rm B}/{\rm nm}^2$.

Optical Axion Electrodynamics:

- θ and $\mathbf{E}\cdot\mathbf{B}$ have identical symmetry properties. They require the breaking of $\mathcal{P}$, $\mathcal{T}$ and all mirrors. Note that there are $\mathcal{PT}$-symmetric phases with mirror symmetry [47]. They do not support the Axion optical ME coupling because mirror forces $\theta = 0$ but they can support other novel optical effect such as the nonreciprocal directional dichroism.
- By adding $\theta(\omega)\frac{e^2}{2\pi hc}\mathbf{E}^\omega\cdot\mathbf{B}^\omega$ into the Lagrangian, the modified Maxwell's equations read

$$\nabla\cdot\mathbf{E}^\omega = \rho - \frac{e^2}{2\pi hc}\nabla\theta(\omega)\cdot\mathbf{B}^\omega \tag{1}$$

$$\nabla\times\mathbf{B}^\omega = \partial_t\mathbf{E}^\omega + \mathbf{j}^\omega + \frac{e^2}{2\pi hc}(\nabla\theta(\omega)\times\mathbf{E}^\omega + \partial_t\theta(\omega)\mathbf{B}^\omega) \tag{2}$$

  The other equations (the Gauss's law for magnetism and the Faraday's law) are unchanged.
- The low frequency limit is defined as frequencies below the magnetic gap at the surface Dirac point, which is typically $\sim$ 10 meV in magnetic topological insulators. Therefore, according to this definition, terahertz light is in the low frequency limit.

- According to Ref. [33], $\theta(\omega)$ is given by

$$\theta(\omega) = \pi\frac{2h}{e^2}\frac{1}{3}(2\alpha(\omega)_{xx} + \alpha(\omega)_{zz}), \tag{3}$$

$$\alpha_{xx}(\omega) = \frac{e^2}{\hbar L}\sum_{\mathrm{o,u}}\int d^2\mathbf{k}\frac{\varepsilon_{\mathrm{uo}}}{\varepsilon_{\mathrm{uo}} - \hbar\omega}\ \mathrm{Im}[\frac{\hbar^2\langle \mathrm{o}|\hat{v}^x|\mathrm{u}\rangle\langle \mathrm{u}| - \frac{1}{2}(\hat{v}^y\hat{r}^z + \hat{r}^z\hat{v}^y) + \hat{m}^{\mathrm{s}}_x|\mathrm{o}\rangle}{\varepsilon_{\mathrm{uo}}^2}], \tag{4}$$

$$\alpha_{zz}(\omega) = \frac{e^2}{\hbar L}\sum_{\mathrm{o,u}}\int d^2\mathbf{k}\frac{\varepsilon_{\mathrm{uo}}}{\varepsilon_{\mathrm{uo}} - \hbar\omega}\ \mathrm{Im}[\frac{\frac{\hbar^2}{2}((\langle \mathrm{o}|\hat{r}^z|\mathrm{u}\rangle\langle \mathrm{u}|\hat{v}^x\hat{v}^y|\mathrm{o}\rangle - \langle \mathrm{o}|\hat{r}^z\hat{v}^x|\mathrm{u}\rangle\langle \mathrm{u}|\hat{v}^y|\mathrm{o}\rangle}{\varepsilon_{\mathrm{uo}}^2}$$
$$\frac{-(x \leftrightarrow y)) + \hbar^2\langle \mathrm{o}|\hat{v}^z|\mathrm{u}\rangle\langle \mathrm{u}|\hat{m}^{\mathrm{s}}_z|\mathrm{o}\rangle}{\varepsilon_{\mathrm{uo}}^2}] \tag{5}$$

where L is the sample thickness, $\varepsilon_{\mathrm{uo}}(\mathbf{k})$ is the energy difference between occupied (o) and unoccupied (u) states, $\hat{v}_x$ and $\hat{v}_y$ are velocity operators, $\hat{r}_z$ is the position operator along z, and $\hat{m}^{\mathrm{s}}$ is the spin operator.

- To get the Berry curvature real space dipole, we start from $\alpha(\omega)_{xx}$ (because the traceless part is small, $\theta(\omega) \simeq \pi\frac{2h}{e^2}\alpha(\omega)_{xx}$.).

$$\begin{aligned}
\alpha(\omega)_{xx} &= \frac{e^2}{\hbar L}\sum_{\mathrm{o,u}}\int d^2\mathbf{k}\frac{\varepsilon_{\mathrm{uo}}}{\varepsilon_{\mathrm{uo}} - \hbar\omega}\ \mathrm{Im}[\frac{\hbar^2\langle \mathrm{o}|\hat{v}^x|\mathrm{u}\rangle\langle \mathrm{u}|\hat{v}^y\hat{r}^z|\mathrm{o}\rangle}{\varepsilon_{\mathrm{uo}}^2}] \\
&= \frac{e^2}{\hbar L}\sum_{\mathrm{o,u}}\int d^2\mathbf{k}\frac{\varepsilon_{\mathrm{uo}}}{\varepsilon_{\mathrm{uo}} - \hbar\omega}\ \mathrm{Im}[\frac{\hbar^2\langle \mathrm{o}|\hat{v}^x|\mathrm{u}\rangle\sum_{\mathrm{p}}\langle \mathrm{u}|\hat{v}^y|\mathrm{p}(\mathbf{k})\rangle\langle \mathrm{p}(\mathbf{k})|\hat{r}^z|\mathrm{o}\rangle}{\varepsilon_{\mathrm{uo}}^2}] \\
&\simeq \frac{e^2}{\hbar L}\sum_{\mathrm{o,u}}\int d^2\mathbf{k}\frac{\varepsilon_{\mathrm{uo}}}{\varepsilon_{\mathrm{uo}} - \hbar\omega}\ \langle\hat{r}^z\rangle_{\mathrm{o}}\mathrm{Im}[\frac{\hbar^2\langle \mathrm{o}|\hat{v}^x|\mathrm{u}\rangle\sum_{\mathrm{p}}\langle \mathrm{u}|\hat{v}^y|\mathrm{p}(\mathbf{k})\rangle\,\delta_{\mathrm{po}}}{\varepsilon_{\mathrm{uo}}^2}] \\
&= \frac{e^2}{\hbar L}\sum_{\mathrm{o,u}}\int d^2\mathbf{k}\frac{\varepsilon_{\mathrm{uo}}}{\varepsilon_{\mathrm{uo}} - \hbar\omega}\ \langle\hat{r}^z\rangle_{\mathrm{o}}\mathrm{Im}[\frac{\hbar^2\langle \mathrm{o}|\hat{v}^x|\mathrm{u}\rangle\langle \mathrm{u}|\hat{v}^y|\mathrm{o}\rangle}{\varepsilon_{\mathrm{uo}}^2}] \\
&= \frac{e^2}{2\hbar L}\sum_{\mathrm{o,u}}\int d^2\mathbf{k}\ \frac{\varepsilon_{\mathrm{uo}}(\mathbf{k})}{\varepsilon_{\mathrm{uo}}(\mathbf{k}) - \hbar\omega}\ \langle\hat{r}^z\rangle_{\mathrm{o}}\Omega_{\mathrm{uo}}
\end{aligned} \tag{6}$$

Therefore, the Berry curvature real space dipole is a good approximation when the wavefunction of the electronic states is concentrated in a particular layer ($\langle\mathrm{p}(\mathbf{k})|\hat{r}^z|\mathrm{o}\rangle \simeq \delta_{\mathrm{po}}\langle\hat{r}^z\rangle_{\mathrm{o}}$). In $MnBi_2Te_4$, because it is a vdW layered material, the interlayer coupling is expected to be relatively weak. Hence, the wavefunction of the electronics states is relatively localized.

Free energy analysis: Similar to previous works [4, 11], we expand the system's free energy in the presence of light. Here we assume the light propagates along $\hat{\mathbf{z}}$.

$$\delta F = \beta\mathbf{M}\cdot[\mathbf{E}^*\times\mathbf{E}] + \gamma\Phi_{\mathrm{chiral}}[\mathbf{E}^*\times\mathbf{E}]\cdot\hat{\mathbf{q}} + \xi L_z[\mathbf{E}^*\times\mathbf{E}]\cdot\hat{\mathbf{z}}, \tag{7}$$

where $\mathbf{E}$ and $\hat{\mathbf{q}}$ are the electric field and unit wavevector of light; $\mathbf{M}$, Φ_{chiral} and $\mathbf{L}$ are the order parameters for FM, chiral crystals and AFM, respectively; β, γ and ξ are the corresponding coupling tensors. First, we explain how each term is constructed. The guiding principle [52] is that a valid free energy term must be invariant under all symmetries. For instance, $\mathbf{M}$ is odd under $\mathcal{T}$ but even under $\mathcal{P}$; one can check that the same is true for $[\mathbf{E}^* \times \mathbf{E}]$, so that $\mathbf{M} \cdot [\mathbf{E}^* \times \mathbf{E}]$ is invariant under both $\mathcal{T}$ and $\mathcal{P}$. Similarly, the spatially-chiral order Φ_{chiral} is odd under $\mathcal{P}$ but even under $\mathcal{T}$, and the same is true for $[\mathbf{E}^* \times \mathbf{E}] \cdot \hat{\mathbf{q}}$. The AFM order L_z (as in even-layered $MnBi_2Te_4$) is odd under both $\mathcal{P}$ and $\mathcal{T}$, and the same is true for $[\mathbf{E}^* \times \mathbf{E}] \cdot \hat{\mathbf{z}}$.

Next, we explain the physical meaning of each term. Importantly, one can check that $\mathbf{E}^* \times \mathbf{E}$, $[\mathbf{E}^* \times \mathbf{E}] \cdot \hat{\mathbf{q}}$, and $[\mathbf{E}^* \times \mathbf{E}] \cdot \hat{\mathbf{z}}$ all flip sign upon reversing light helicity (while keeping the propagation direction invariant). The first term is the energy coupling between M and circularly-polarized light, which is responsible for the helicity-dependent optical control of magnetization observed in FMs [4]. The second term is the energy coupling between spatial chirality and circularly-polarized light, which is responsible for the helicity-dependent optical control of spatial chirality observed in asymmetrical chemical reactions [10] and gyrotropic electronic order [11]. The last term is the energy coupling between the fully-compensated AFM order and circularly-polarized light, which is responsible for the helicity-dependent optical control of the fully-compensated AFM order, achieved for the first time in even-layered $MnBi_2Te_4$ here. The coupling constant ξ directly arises from the optical Axion electrodynamics, as we demonstrated from the data above.

First-principles calculations: First-principles band structure calculations were performed using the projector augmented wave method as implemented in the VASP package within the generalized gradient approximation (GGA) schemes. $9 \times 9 \times 1$ Monkhorst-Pack k-point meshes with an energy cutoff of 400 eV were adapted for the Brillouin zone integration. Experimentally determined lattice parameters were used. In order to treat the localized Mn $3d$ orbitals, we follow previous first-principles works [15, 51] on $MnBi_2Te_4$ and used an onsite $U = 5.0$ eV. The Wannier model for the few-layered $MnBi_2Te_4$ was built using the Bi p, Te p and Mn d orbitals. All optical response functions were calculated based on the Wannier model.

[48] Yan, J.-Q. *et al.* Crystal growth and magnetic structure of $MnBi_2Te_4$. *Phys. Rev. Mater.* **3**, 064202 (2019).

[49] Zhao, S. Y. F. *et al.* Emergent Interfacial Superconductivity between Twisted Cuprate Superconduc-

tors. Preprint at arXiv:2108.13455 (2021).

[50] Thiel, L. *et al.* Probing magnetism in 2D materials at the nanoscale with single-spin microscopy. *Science* **364**, 973–976 (2019).

[51] Otrokov, M. M. *et al.* Unique thickness-dependent properties of the van der Waals interlayer antiferromagnet $MnBi_2Te_4$ films. *Phys. Rev. Lett.* **122**, 107202 (2019).

[52] Toledano, J.-C. & Toledano, P. *The Landau theory of phase transitions: application to structural, incommensurate, magnetic and liquid crystal systems* (World Scientific, 1987).

[53] Ahn, J., Guo, G.-Y., Nagaosa, N. & Vishwanath, A. Riemannian geometry of resonant optical responses. *Nature Phys.* **18**, 290-295 (2022).

Data availability: The data that support the plots within this paper and other findings of this study are available from the corresponding author upon reasonable request.

Acknowledgement: We gratefully thank Xiaodong Xu and Tiancheng Song for sharing experience on CD setup and Manfred Fiebig for providing the Cr_2O_3 bulk crystals. We also thank Yang Gao, Bertrand I. Halperin, Pavon Hosur, and Philip Kim for helpful discussions. Work in the SYX group was supported through NSF Career (Harvard fund 129522) DMR-2143177. SYX acknowledge the Corning Fund for Faculty Development. SYX, JA, QM, AV acknowledge support from the Center for the Advancement of Topological Semimetals, an Energy Frontier Research Center funded by the U.S. Department of Energy (DOE) Office of Science, through the Ames Laboratory under contract DE-AC0207CH11358. The sample fabrication in the QM group was supported by the NSF Career DMR-2143426 and the (CIFAR) Azrieli Global Scholars program. CT acknowledges support from the Swiss National Science Foundation under project P2EZP2_191801. YFL, SYX, and DCB were supported by the STC Center for Integrated Quantum Materials (CIQM), NSF Grant No. DMR-1231319. This work was performed in part at the Center for Nanoscale Systems (CNS) Harvard University, a member of the National Nanotechnology Coordinated Infrastructure Network (NNCI), which is supported by the National Science Foundation under NSF award no.1541959. Work at UCLA was supported by the U.S. Department of Energy (DOE), office of Science, office of Basic Energy Sciences under Award Number DE-SC0021117. The work at Northeastern University was supported by the Air Force Office of Scientific Research under award number FA9550-20-1-0322, and it benefited from the computational resources of Northeastern University's Advanced Scientific Computation Center (ASCC) and the Discovery Cluster. TRC was supported by the Young Scholar Fellowship Program from the MOST in Taiwan, under a MOST grant for the Columbus Program, no. MOST110-2636-M-006-016, NCKU, Taiwan, and National Center for Theoretical Sciences, Taiwan. Work at NCKU was supported by the MOST, Taiwan, under grant no.MOST107-2627-E-006-001 and Higher Education Sprout Project at NCKU. HZL was supported by the National Natural Science Foundation of China (11925402), Guangdong province (2016ZT06D348, 2020KCXTD001), and the Science, Technology and Innovation Commission of Shenzhen Municipality (ZDSYS20170303165926217, JCYJ20170412152620376, KYTDPT20181011104202253), and Center for Computational Science and Engineering of SUSTech. K.W. and T.T. acknowledge support from JSPS KAKENHI (Grant Numbers 19H05790, 20H00354 and 21H05233). X-YZ, Y-XW, and BBZ acknowledge support from the NSF award No. ECCS-2041779.

Author contributions: JXQ performed the optical measurements and analyzed data with help from CT and HCL. JXQ performed the transport measurements with help from AG. AG fabricated the 2D $MnBi_2Te_4$ samples with help from JXQ, HCL, YFL, DB, TD, SCH, and QM. CH and NN grew the bulk $MnBi_2Te_4$ single crystals. JA and AV developed the theory of optical Axion electrodynamics with discussions with SYX. BG and JA made first-principles calculations with helps BS from under supervisions of HS, TRC, AB, and AV. ZHG and HZL did model simulations. DCB performed transmission electron microscope measurements. X-YZ, Y-XW, and BBZ performed nitrogen-vacancy center magnetometry experiments. KW and TT grew the bulk hBN single crystals. SYX, JXQ and QM wrote the manuscript with input from all authors. JXQ came up with the idea of optical induction of AFM. SYX supervised the project and was responsible for the overall direction, planning and integration among different research units.

Competing financial interests: The authors declare no competing financial interests.

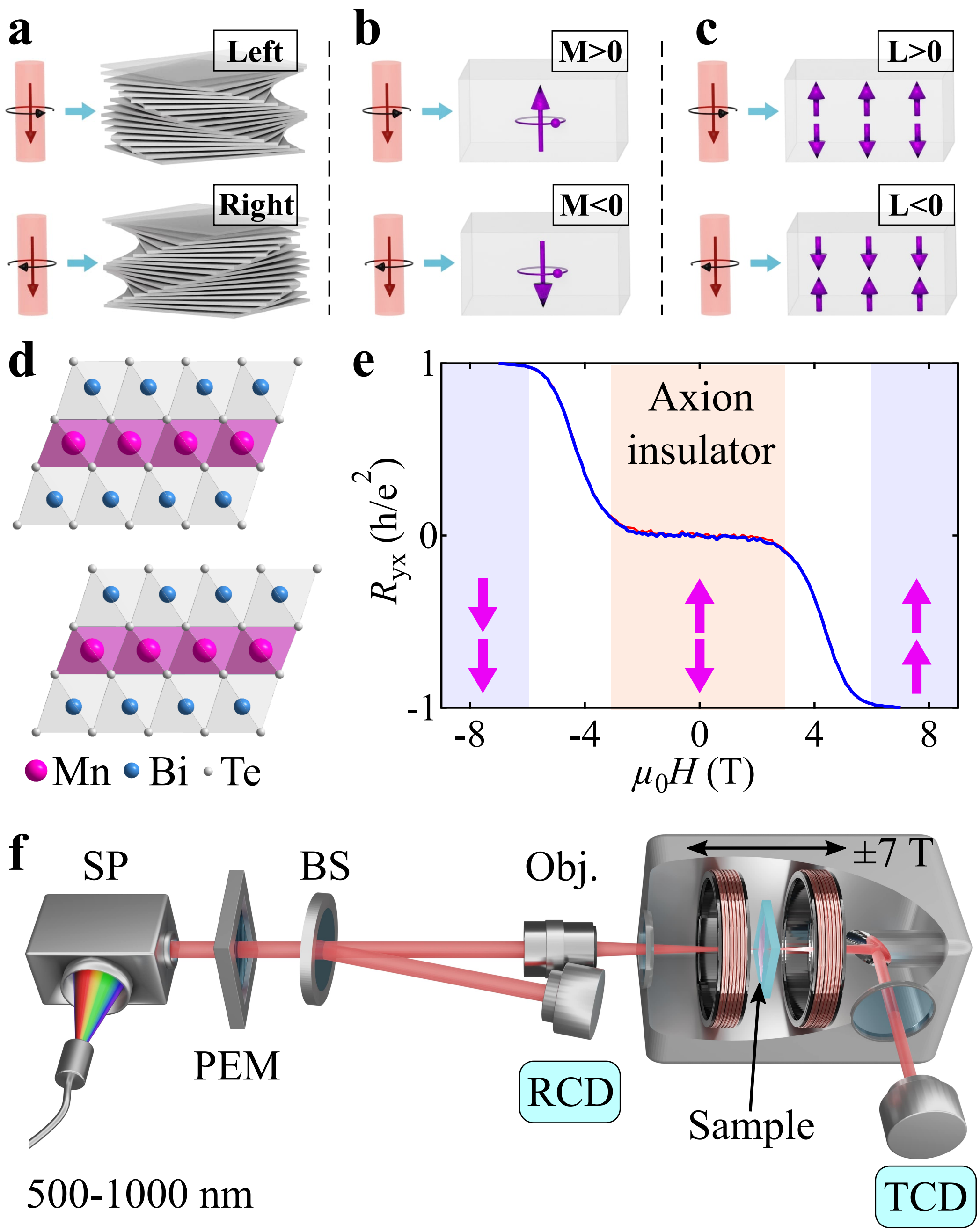

FIG. 1: **Helicity-dependent optical control of quantum matter and introduction to $MnBi_2Te_4$.** **a,b,** Previous studies have demonstrated helicity-dependent optical control of spatial chirality and magnetization [4, 10, 11]. **c,** We report the surprising observation of helicity-dependent optical control of fully-compensated antiferromagnetic (AFM) order. **d,** Lattice structure of $MnBi_2Te_4$. **e,** Hall resistivity of our 6SL $MnBi_2Te_4$ with the layered magnetic state shown by the pink arrows. For each state, two out of six layers are pictured for simplicity. The Axion insulator state is realized by the fully-compensated AFM near $B = 0$. **f,** Our circular dichroism set up. SP, PEM, BS, Obj. are spectrometer, photoelastic modulator, beam-splitter, and objective, respectively.

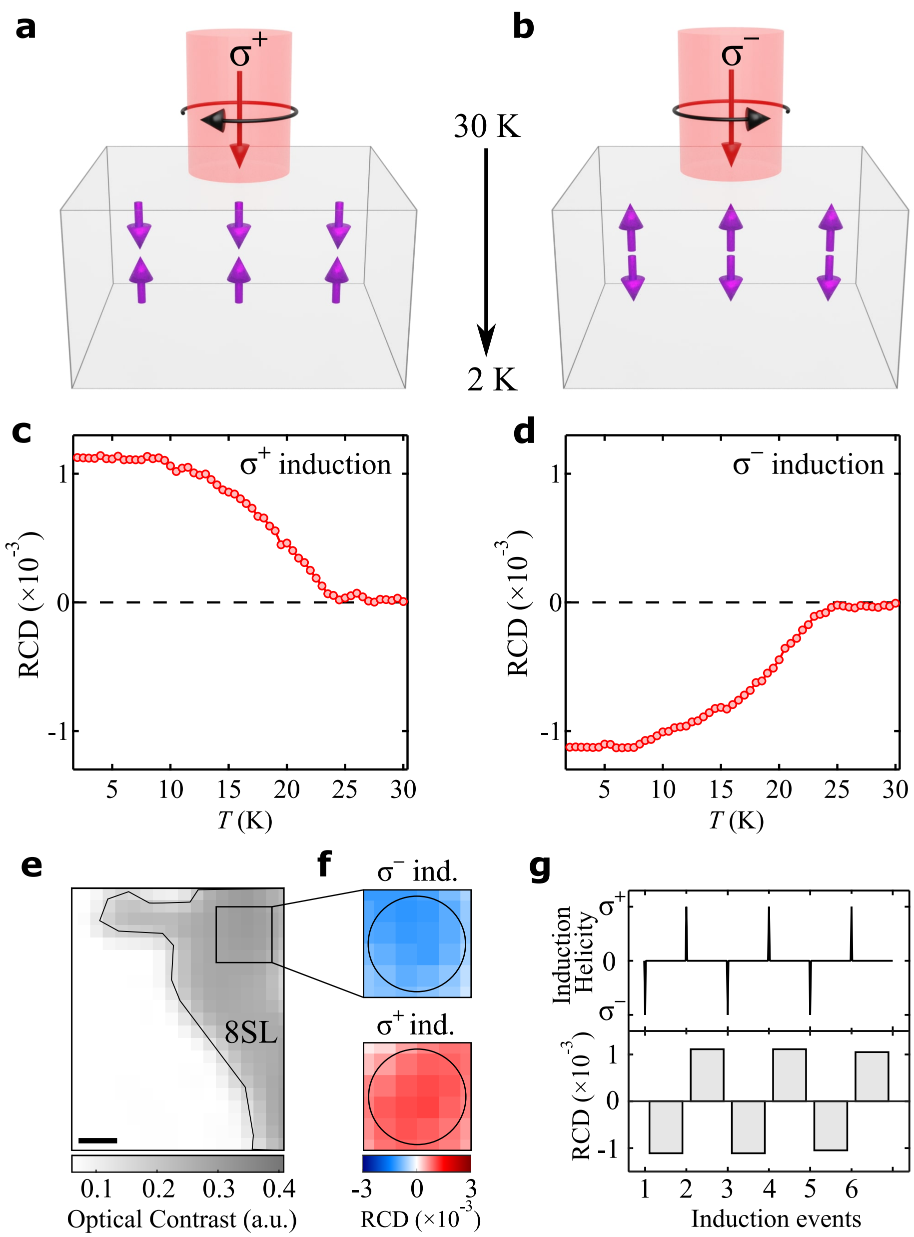

FIG. 2: **Optical induction in a 2D topological antiferromagnet.** **a,** We shine σ^+ circularly-polarized induction light ($\lambda_{\text{induction}} = 840$ nm, $P_{\text{induction}} \simeq 1$ mW) on the sample S1 (8SL $MnBi_2Te_4$ flake on a sapphire substrate) while lowering its temperature from $T = 30$ K to 2 K. **c,** Upon reaching 2 K, we turn off the induction light and measure the reflection CD (RCD) with the detection light at $\lambda_{\text{detection}} = 946$ nm and $P_{\text{detection}} \simeq 30$ μW. Surprisingly, we observe a significant RCD at $B = 0$. Upon warming up, the RCD vanishes above T_{N}. **b,d,** Same as panels (**a,c**) except that we shine σ^- circularly-polarized induction light on the sample while lowering its temperature from $T = 30$ K to 2 K. **e,** Spatial mapping of the optical contrast near the 8SL flake. Scale bar: 2 μm. **f,** RCD signal after induction with opposite helicity. The circle marks the spot subject to the induction light while cooling. **g,** RCD signal at the center of the circle in panel (**f**) after consecutive induction processes with opposite helicity.

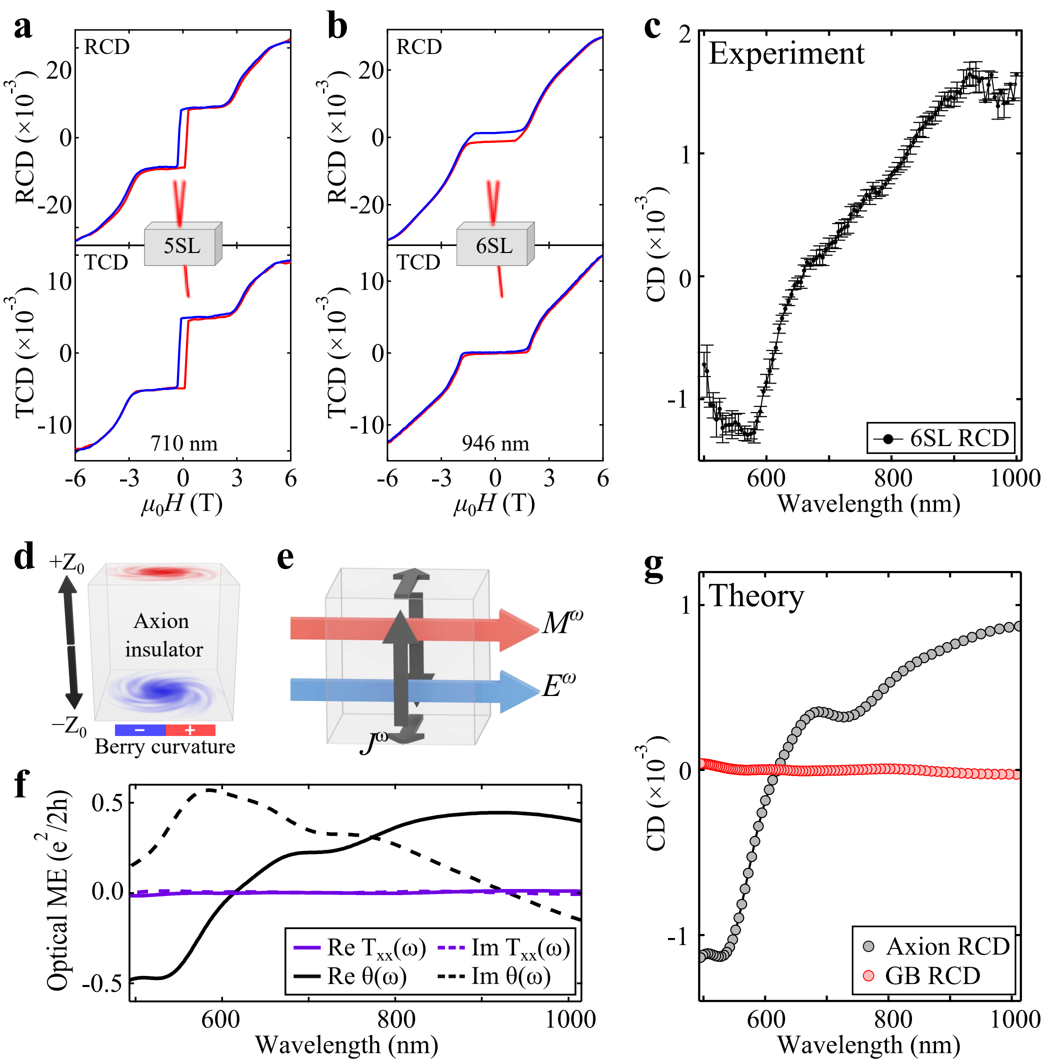

FIG. 3: **Unique reflection and transmission properties and observation of the Axion CD. a,b,** Simultaneous RCD and TCD measurements of the 5SL (panel **a**) and 6SL (panel **b**) in sample-S3. **c,** Wavelength dependence of RCD data at $B = 0$ for 6SL. **d,** Schematic illustration of the Berry curvature real-space dipole. Electrons at opposite positions ($\pm Z$) in even-layered $MnBi_2Te_4$ have opposite Berry curvature. **e,** the Axion optical ME coupling can be visualized an itinerant electron circulation in response to electric field as a consequence of the Berry curvature real-space dipole. **f,** Optical Axion $\theta(\omega)$ and gyrotropic birefringence (T_{xx}) of 6SL $MnBi_2Te_4$ calculated from first-principles band structures. **g,** Theoretically computed Axion CD and GB CD.

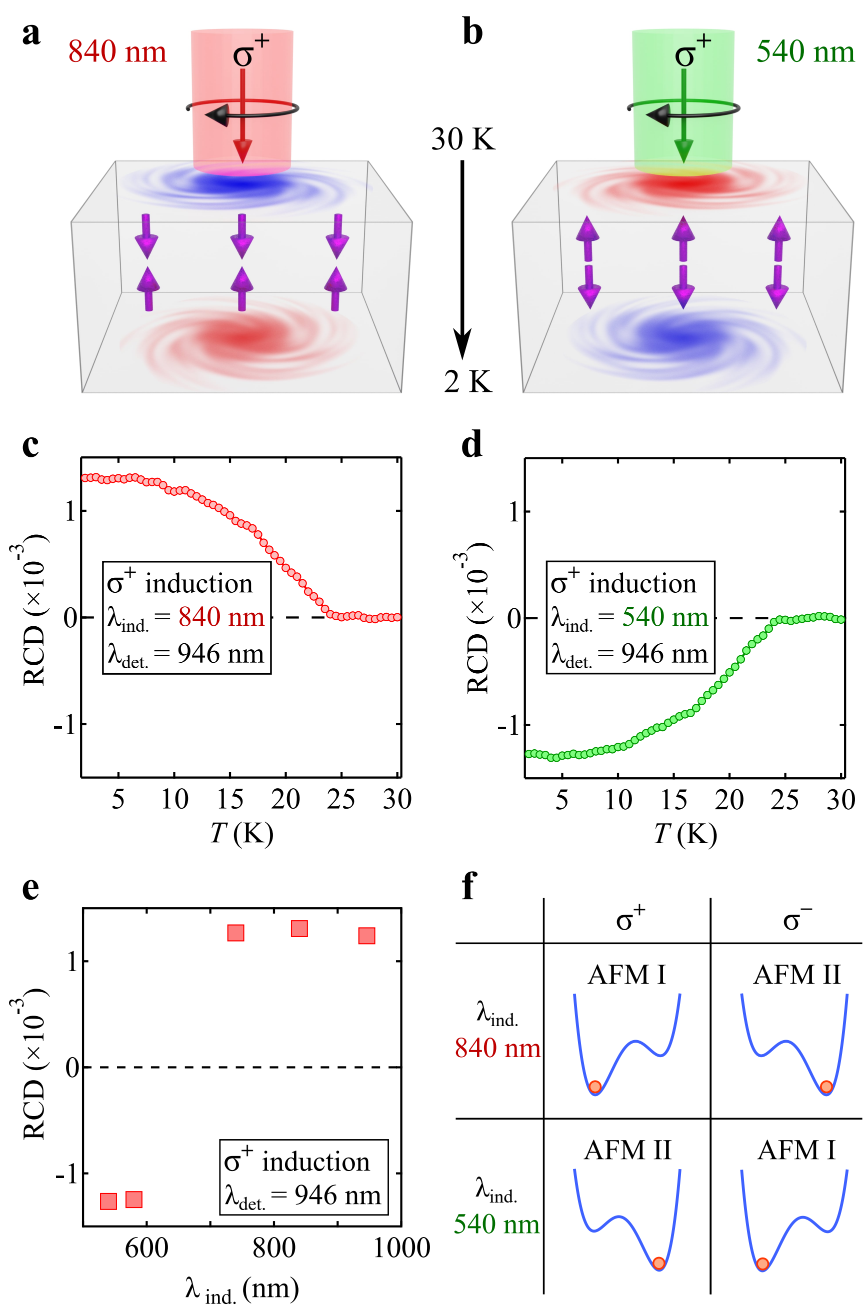

FIG. 4: **Observation of the Axion induction. a,c,** We shine σ^+ circularly-polarized induction light ($\lambda_{\text{induction}}$ = 540 nm, $P_{\text{induction}} \simeq 1$ mW) on the 8SL $MnBi_2Te_4$ flake (sample-S1) while lowering its temperature from T = 30 K to 2 K (panel **a**). We turn off the induction light and measure the RCD with $\lambda_{\text{detection}}$ = 946 nm while warming up (panel **c**). **b,d,** Same as panels (**a,c**) except the induction wavelength is $\lambda_{\text{induction}}$ = 840 nm. **e,** Induction wavelength dependence. To consistently compare how induction wavelength $\lambda_{\text{induction}}$ influences the results of induction, we fix all other experimental parameters including induction helicity (fixed at σ^+) and detection wavelength (fixed at $\lambda_{\text{detection}}$ = 946 nm) and we only vary $\lambda_{\text{induction}}$. **f,** Free energy diagrams summarize the optical control of the AFM order in even-layered $MnBi_2Te_4$ with light helicity and wavelength.

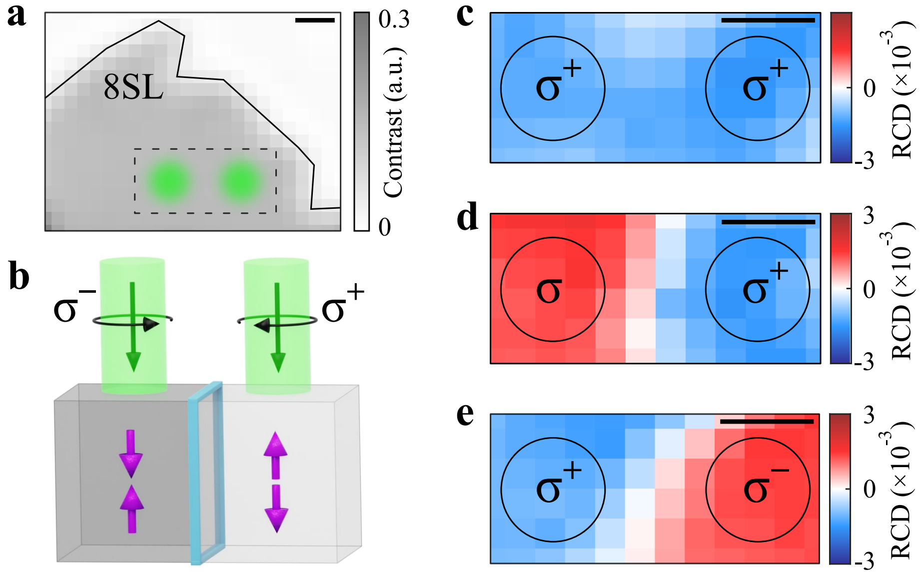

FIG. 5: **Optical creation of AFM domain wall by double Axion induction.** **a,** We shine two close-by circularly-polarized induction light beams on an 8SL $MnBi_2Te_4$ flake (sample-S5). Scale bar: 2 μm. $\lambda_{\mathrm{induction}}$ = 540 nm. **b,** Schematic illustration of the double induction leading to an AFM domain wall. **c-e,** RCD mappings of the area subject to the double induction with (σ^+, σ^+), (σ^-, σ^+), and (σ^+, σ^-), respectively.

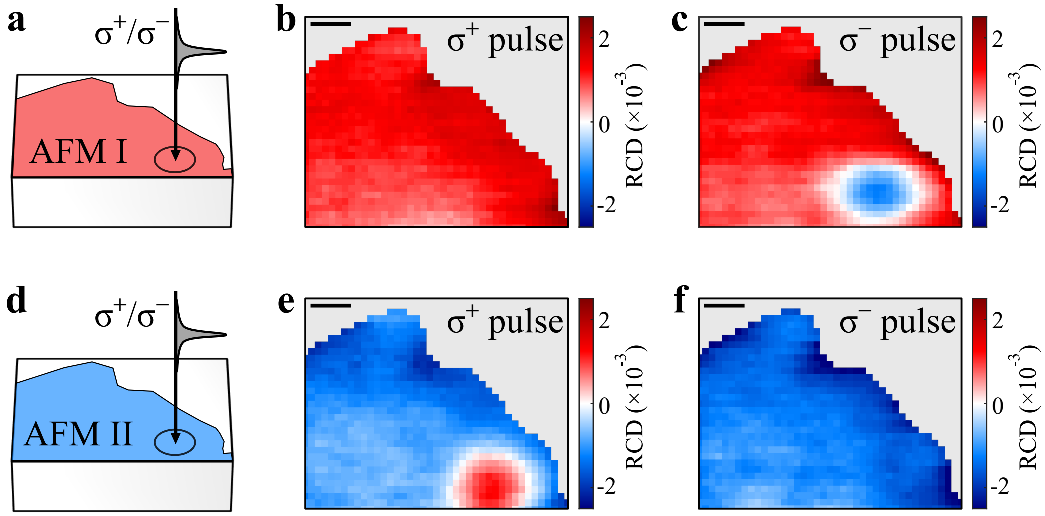

FIG. 6: **Direct optical switch of AFM order by ultrafast pulse with circularly polarization.** **a,** Schematic illustration of the entire 8SL sample (sample-S1) in the same AFM domain (achieved by sweeping the B field from +7 T to 0 T). We shine circularly-polarized ultrafast pulsed light while keeping the sample at T = 18 K (below T_{N} = 25 K). **b,c,** RCD maps after shining circularly-polarized ultrafast pulsed light. **d-f**, The same as panels (**a-c**) but for the opposite AFM domain prepared by sweeping the B field from −7 T to 0 T. See additional data in SI.II.4. Scale bar: 2 μm.

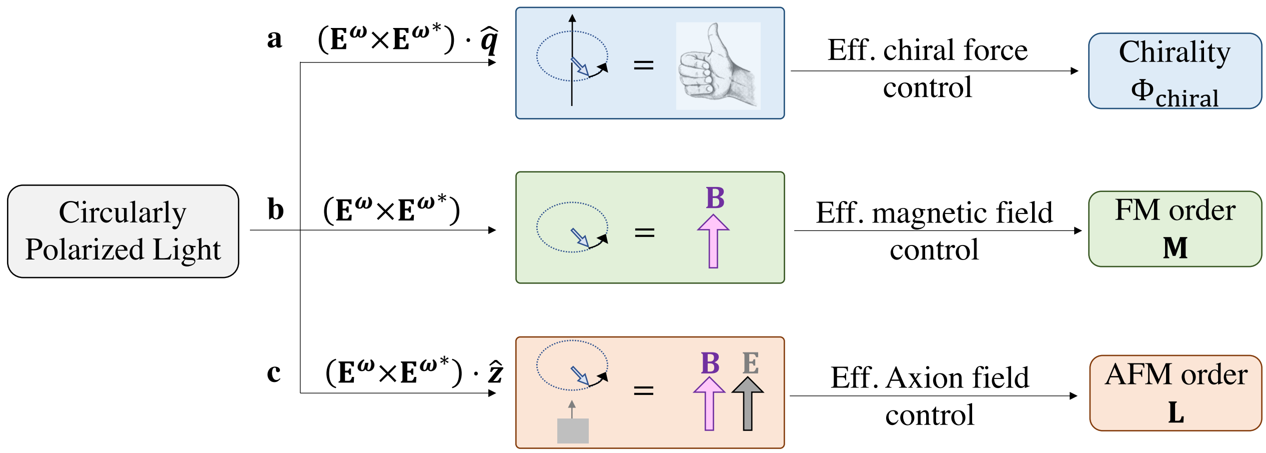

Extended Data Fig. 1: **Distinct mechanism for the three classes of helicity-dependent optical control.** $(\mathbf{E}^{\omega}\times\mathbf{E}^{\omega*})\cdot\hat{\mathbf{q}}$, $(\mathbf{E}^{\omega}\times\mathbf{E}^{\omega*})$, and $(\mathbf{E}^{\omega}\times\mathbf{E}^{\omega*})\cdot\hat{\mathbf{z}}$ are symmetry-equivalent to chirality, **B** and $\mathbf{E}\cdot\mathbf{B}$, respectively.

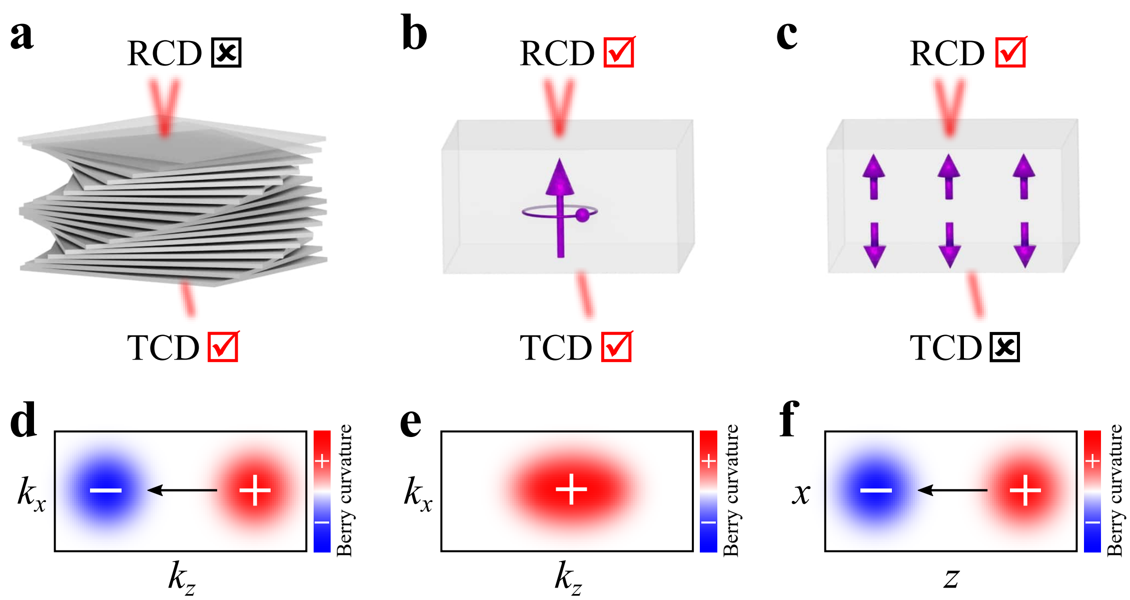

Extended Data Fig. 2: **Three classes of CD in chiral crystals, ferromagnets and $\mathcal{PT}$-symmetric AFM. a-c**, Chiral crystals, ferromagnets and $\mathcal{PT}$-symmetric AFM feature distinct nontrivial interactions with circularly-polarized light. They can only be distinguished by their transmission and reflection properties. **d-f**, Equally importantly, when bands with nontrivial topology or giant Berry curvature occur in these three classes of materials, the respective CD can dominantly arise from the Berry curvature properties, namely the Berry curvature k space dipole, the total Berry curvature, and the Berry curvature real space dipole, respectively.

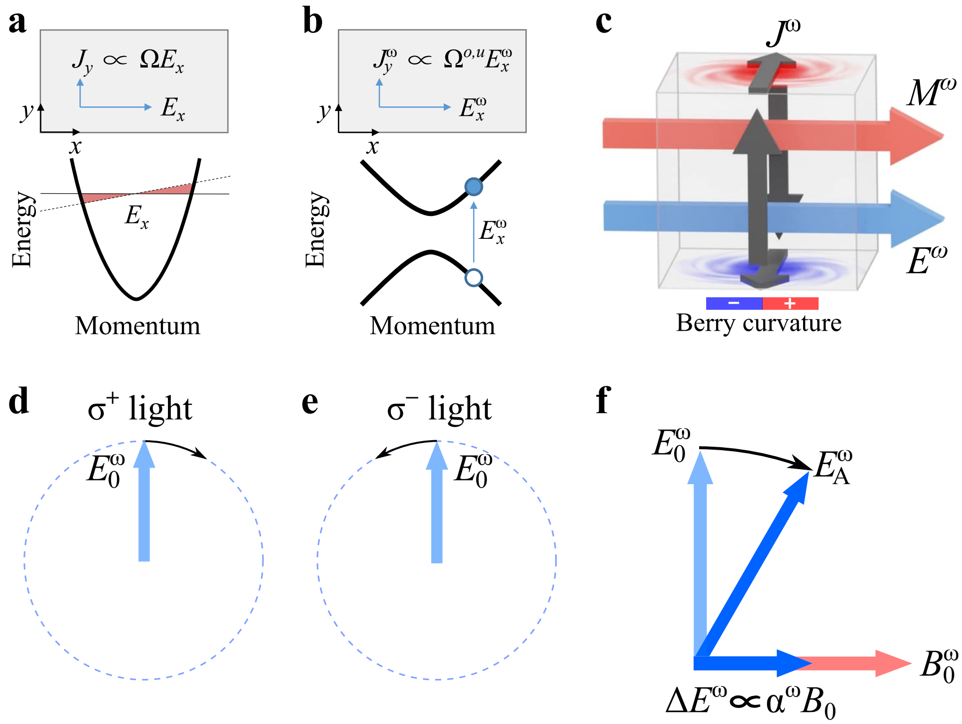

Extended Data Fig. 3: **a,** The Berry curvature causes transverse electron motion in response to an external DC E field. **b,** Analogously, the inter-band Berry curvature causes a transverse electron motion in response to light's E^ω field upon an interband transition. Ref. [53] provides a detailed theoretical analysis for the clear geometrical origin of the inter-band Berry curvature. **c,** The Berry curvature induced optical ME coupling can be visualized an itinerant electron circulation in response to electric field. Specifically, upon the application of an electric field E^ω, Berry curvature leads to transverse electron motion. Because of the Berry curvature at $\pm Z$ is opposite, the transverse motions of electrons at $\pm Z$ are in opposite directions. This in turn leads to an itinerant electron circulation J^ω, which is equivalent to magnetization M^ω. **d,e,** Rotation of electric field E_0^ω for $\sigma^\pm$ light. **f,** Light's magnetic field B^ω can lead to an electric polarization $P_0^\omega = \alpha(\omega) B_0^\omega$ through the optical ME effect, which rotates light's electric field E^ω. Suppose this rotation is in the clockwise direction. Then, this additional clockwise rotation would be along the same direction as the intrinsic rotation (also clockwise) for σ^+ light but opposite to the intrinsic rotation (counter-clockwise) for σ^- light. This provides an intuitive picture for why $\sigma^\pm$ light can behave differently in an Axion insulator, a prerequisite for nonzero CD.

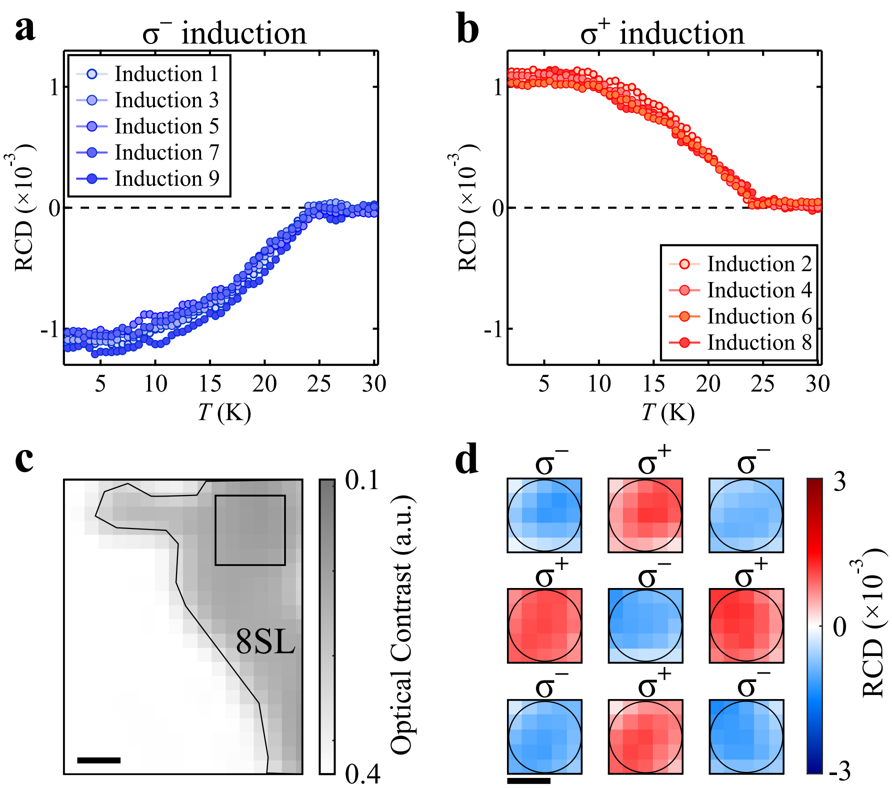

Extended Data Fig. 4: **Reproducible RCD measurements for nine consecutive inductions with alternating induction helicities. a,** RCD as a function of temperature while warming up after induction with σ^- light. **b,** Same as panel (**a**) but after induction with σ^+ light. **c,** Spatial mapping of the optical contrast near the 8SL $MnBi_2Te_4$ flake. The square box marks the region for induction experiments. **d,** RCD map after induction with opposite helicity. The circle marks the spot that is subject to the induction light while cooling; The σ^+ and σ^- on each small panel denotes the helicity of the induction light. Experimental parameters used for data in this figure: $\lambda_{\text{induction}} = 840$ nm, $P_{\text{induction}} \simeq 1$ mW; $\lambda_{\text{detection}} = 946$ nm, $P_{\text{detection}} \simeq 30$ μW. Scale bars for panels (**e,f**) are 2 μm.

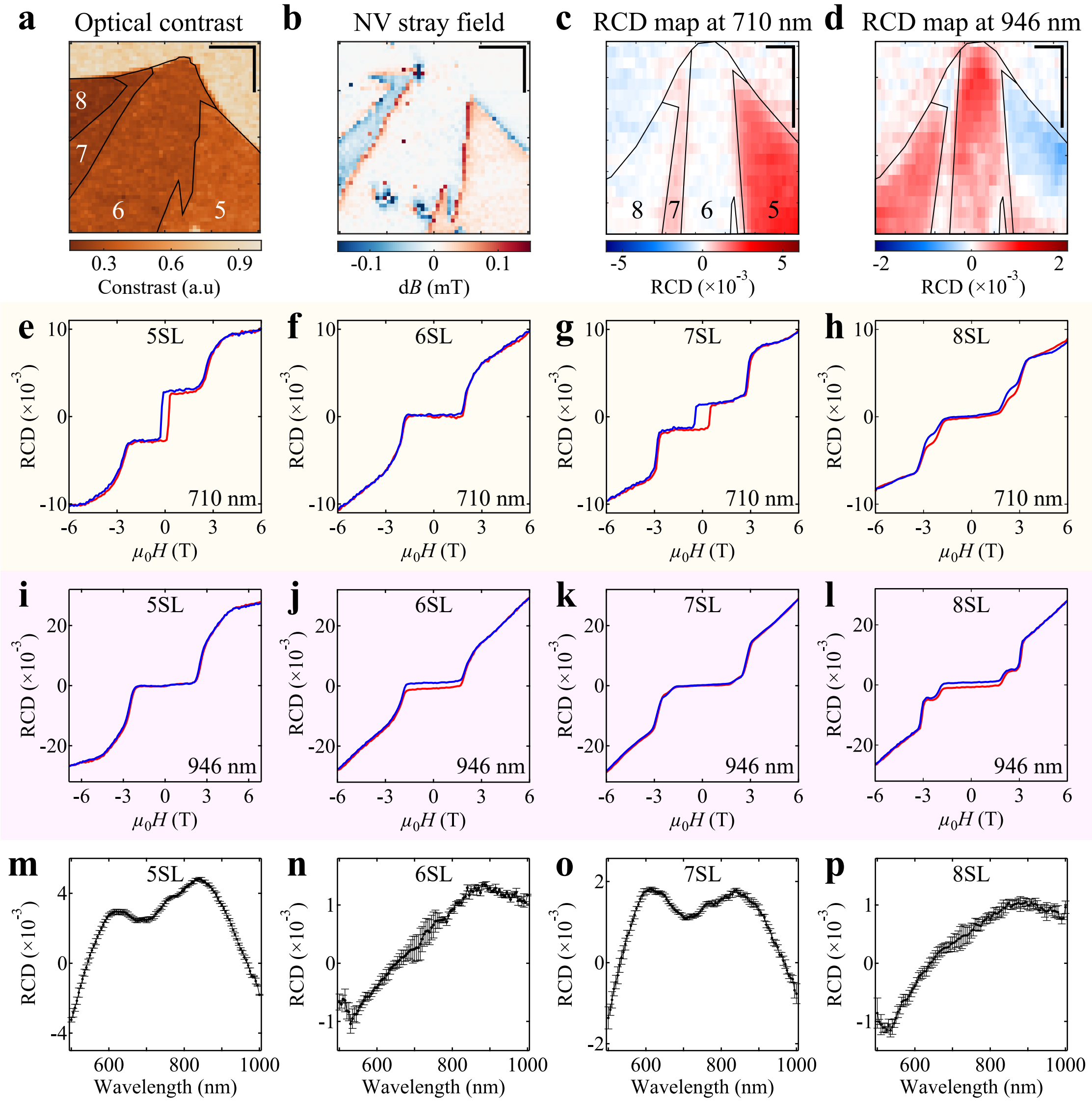

Extended Data Fig. 5: **Circular dichroism in 2D $MnBi_2Te_4$. a,** Optical contrast of sample-S2 on diamond structure, which consists of four connected flakes of 5SL, 6SL, 7SL and 8SL. **b,** Nitrogen vacancy center measured stray magnetic field of sample S2. **c,** RCD spatial mapping at $B = 0$ using $\lambda_{\text{detection}} = 710$ nm. The sample was cooled down with a finite B field and the B field was ramped to zero before the measurements. **d,** Same as panel **c** but using $\lambda_{\text{detection}} = 946$ nm with. No optical induction was performed in panels **c,d**. Scale bars (horizontal and vertical lines) are all 5 μm. We note that the NV and CD measurements were performed in different setups. Hence the spatial mappings (**b** and **c,d**) are rotated with respect to each other. **e-h,** Magnetic hysteresis of RCD for 5SL, 6SL, 7SL and 8SL measured at $\lambda_{\text{detection}} = 710$ nm. **i-l,** Same as panels (**e-h**) but measured at $\lambda_{\text{detection}} = 946$ nm. **m-p,** RCD spectra at $B = 0$ for 5-8SL. The spectrum strongly depends on the evenness or oddness of the layer number, consistent with the different physical origins of the CDs in even and odd layers. It is interesting to note that ~ 700 nm is the symmetric (antisymmetric) point for odd (even) layers.

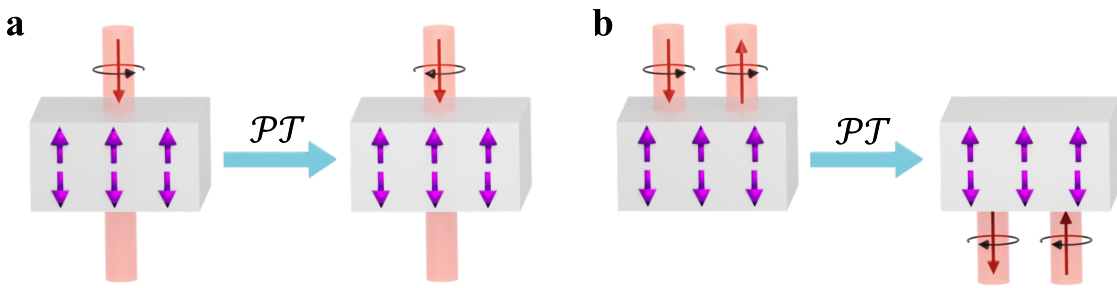

Extended Data Fig. 6: **Symmetry analysis for CD in $\mathcal{PT}$-symmetric AFM. a,** σ^- light transmitting through a sample. Upon $\mathcal{PT}$ inversion, the AFM remains invariant and the light path also stays the same, but light helicity is reversed. As such, $\mathcal{PT}$ enforces the transmission for $\sigma^\pm$ to be identical, which means TCD = 0. **b,** σ^- light reflecting off a sample. Upon $\mathcal{PT}$ inversion, the AFM remains invariant but the reflection is changed to the bottom surface. This means that $\mathcal{PT}$ does not impose any constraint on RCD experiments, because RCD compares the reflections of $\sigma^\pm$ lights from the same side of the sample. Carrying out the same analysis exhaustively confirms that there is no symmetry that can relate the reflections of light with opposite helicity while keeping the AFM invariant. Therefore, RCD is allowed.

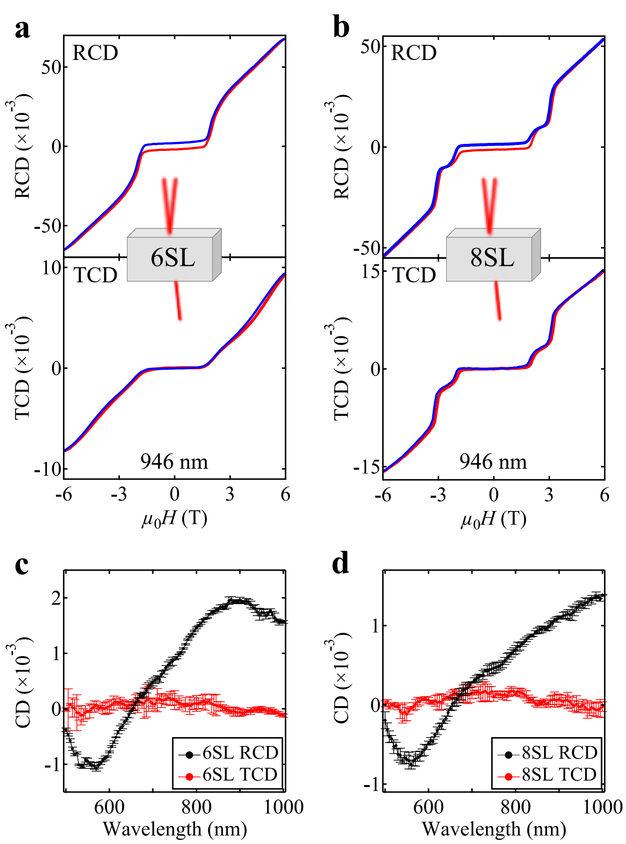

Extended Data Fig. 7: **RCD** *vs.* **TCD measurements of the 6SL and 8SL $MnBi_2Te_4$ in sample-S1. a,b,** RCD and TCD magnetic hysteresis measurements at 946 nm. **c,** RCD and TCD spectra at $B = 0$.